Contents lists available at ScienceDirect

# Solar Energy

# Highly efficient quasi-cubic structured perovskite for harvesting energy from artificial indoor LED light source

Ranbir Singh [a,*], Vivek Kumar Shukla [b], Mritunjaya Parashar [c], Vikrant Sharma [d], Satinder Kumar Sharma [a]

[a] *School of Computing and Electrical Engineering (SCEE), Indian Institute of Technology (IIT) Mandi, Mandi, Himachal Pradesh 175005, India*
[b] *Department of Applied Physics, School of Vocational Studies and Applied Sciences, Gautam Buddha University, Greater Noida, U.P. 201312, India*
[c] *Department of Physics, University of North Texas, Denton, TX 76207, USA*
[d] *National Institute of Solar Energy (NISE), Gurugram, Haryana 122003, India*

## ARTICLE INFO

## ABSTRACT

Mixed cations-based perovskites have attracted a lot of interest because of their ability to harvest light energy and ambient air stability. Herein, we synthesized mixed methylammonium/formamidinium cations ($MA^+$/$FA^+$) perovskite materials and explored their potential for harvesting energy from the indoor LED light source. The incorporation of $FA^+$ in methylammonium lead iodide ($MAPbI_3$) induces a transition in crystal structure from tetragonal to intermediate quasi-cubic, resulting in a more stable and efficient quasi-cubic perovskite structured morphology. The fabricated photovoltaic devices demonstrated an efficiency of 34.07% with mixed cations compared to the reference $MAPbI_3$ of 28.63% under the indoor LED lamp at 1000 lx. The optimized photovoltaic device has displayed considerable enhancement in short circuit current density ($J_{SC}$) and open-circuit voltage ($V_{OC}$), including lower hysteresis and reduced recombination losses. Furthermore, a detailed study was conducted to determine the impact of quasi-cubic crystal structures on the grains and grain boundaries that exist in the perovskite film. The surface potential (SP), and charge carrier dynamics measurements nearby grain boundaries revealed a significant decrease in defects or trap states. In brief, this work comprehensively puts forward a prospective candidature of quasi-cubic perovskites for the development of photovoltaic technology to harvest indoor light energy.

## 1. Introduction

With the development of internet of things (IoTs), the demand to power up the small electronic gadgets such as Wi-Fi routers, calculators, barcode scanners, smartwatches, and headphones etc., has grown exponentially (Aslam et al., 2020; Dagar et al., 2018; Mathews et al., 2016; Uslu et al., 2020). Most of the sensor nodes require the power of 10–100 μW which can be easily fulfilled by converting the artificial indoor light to electricity. Typically, indoor light luminescence ranges from 200–2000 lx (0.05–0.1mW cm$^{-2}$), which is nearly a thousand times lower than that of one sun illumination (100 mW cm$^{-2}$), making it appropriate for IoTs. In the last decade, 3rd-generation perovskite photovoltaics (PPVs) have demonstrated excellent results for outdoor as well as indoor light harvesting due to their remarkable optical and electrical properties.(Chen et al., 2015; Dagar et al., 2018; Dong et al., 2015; Liu et al., 2018; Nazeeruddin and Snaith, 2015; Park, 2015; Pham et al., 2020; Savenije et al., 2014; Singh et al., 2021; Stranks et al., 2013; Wetzelaer et al., 2015) The photovoltaics made with perovskite materials have made significant development in terms of power conversion efficiencies (PCEs), increasing from 3.8% to 25.5% under one sun condition, and great emphasis has been paid for harvesting indoor light energy.(Green et al., 2021; Kawata et al., 2015; Lee et al., 2021) Owing to indoor light source designs, lighting energy limits its capacity to absorb only in the visible regions resulting in theoretical Shockley–Queisser (S-Q) efficiency of ~52% under white LED light at ~1000 lx.(Venkateswararao et al., 2020) The indoor PPVs (i-PPVs) have crossed a PCE of 30%, outperforming all other current photovoltaic technologies such as silicon and thin-film technologies.(Guo et al., 2021; Lee et al., 2021; Lim et al., 2020; Noh et al., 2020; Saranin et al., 2021) The strategies that focus on high PCE systems in indoor conditions include two major areas: tuning the absorption spectrum of the perovskite with the indoor light source and minimizing the open-circuit voltage ($V_{OC}$)

---

* Corresponding author.
  *E-mail address:* ranbir.iitk@gmail.com (R. Singh).
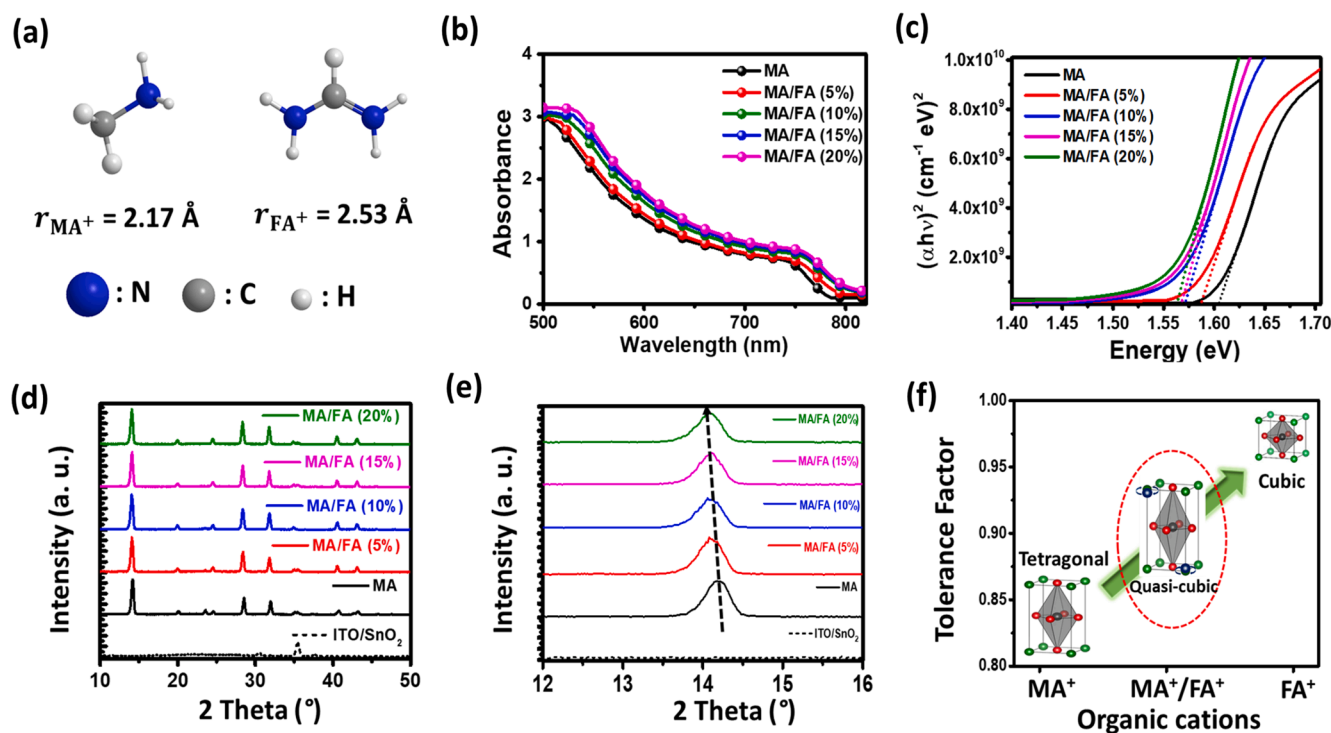
**Fig. 1.** (a) The molecular structure of MAI and FAI with their ionic radii, (b) absorption spectra, (c) Tauc's plot, (d) XRD patterns of all the perovskite films deposited on the ITO/SnO₂ coated glass substrates (e) Zoomed XRD pattern showing shift in (1 1 0) peak position and (f) tolerance factor (TF) and corresponding crystal structure transformation from tetragonal of MAPbI₃ to quasi-cubic of MA/FAPbI₃.

loss. The high value of $V_{OC}$ in i-PPVs is critical since the devices tend to operate at lower voltages because of the higher voltage loss in comparison to the devices operated under one sun conditions.(Lim et al., 2020) The efficiency of i-PPVs is influenced by the energy loss at the bulk and interface of the perovskite/transport layers. When the number of charge carriers is minimal, it becomes much more difficult to recover trapped charges.(Chen et al., 2015) Therefore, enhancing perovskite film crystal quality, limiting non-radiative recombination at the interface, and optimizing the structure of the charge transport layers are anticipated to significantly improve the device efficiency even further. (Cheng et al., 2019; Guo et al., 2017; Muhammad et al., 2022; Ren et al., 2020) Recently, in one of our previously published works, we examined the association of spectral tuning, crystal structure variation from tetragonal to pseudo cubic to cubic, charge carrier mobility, recombination losses, and trap states over a range of methylammonium based i-PPVs, by changing the halide (iodide to bromide) ratio in perovskites namely MAPbI₃, MAPbI₂Br, MAPbIBr₂, and MAPbBr₃.(Singh et al., 2021) It was found that even after crystal structure variation and bandgap tuning close to the ideal bandgap of ~1.90 eV for indoor photovoltaic applications, as well as taking into account higher $V_{OC}$ values in i-PPVs, the current loss was significantly higher. This undermined the slight increase in the $V_{OC}$ which resulted in inferior device performance with the increasing bromide content. However, the trap densities and recombination analysis for the above-mentioned four systems suggested that the pure crystalline phases of perovskites have lower defect densities and thus lower charge carrier recombination. (Singh et al., 2021) Our current efforts are focused on resolving a key open question from the prior work: whether tweaking the 'A'-site cation rather than the halide has the same impact on the various crystal forms and their charge transport methods under indoor illumination.

In the present work, mixed cations FA⁺/MA⁺ perovskite has been optimized for achieving high efficiency under indoor light conditions. The incorporation of FA⁺ in MAPbI₃ perovskite was examined for the crystal structure transformation and their impact on the perovskite film morphology. The fabricated i-PPVs demonstrated a PCE of 34.07% and

$V_{OC}$ of 0.92 V for mixed cations perovskite as compared to reference single cation MAPbI₃ i-PPVs (PCE = 28.63 % and $V_{OC}$ = 0.83 V). In addition, supporting linking studies on morphology using Kelvin probe force microscopy (KPFM), charge carrier recombination losses, and operational stability of the i-PPVs have been conducted to further get a better mechanistic understanding of the influence of quasi-cubic perovskite structure on photovoltaic performances.

## 2. Results and discussion

### 2.1. Photophysical and morphological properties

Different mixed cations MA/FAPbI₃ perovskite were synthesized as per the procedure explained in the experimental section of the supporting information (SI). The mole percentage of the formamidinium (FA⁺) was varied between 0% and 20% in respect of methylammonium (MA⁺) in MAPbI₃ perovskite. The fabricated MAPbI₃, MA₀.₉₅FA₀.₅PbI₃, MA₀.₉FA₀.₁PbI₃, MA₀.₈₅FA₀.₁₅PbI₃, and MA₀.₈FA₀.₂PbI₃ films are denoted as MA, MA/FA (5%), MA/FA (10%), MA/FA (15%), and MA/FA (20%), respectively. The molecular structures of MAI and FAI with their cationic radii are shown in Fig. 1a. Although the 'A'-site cation has little effect on band structure and it mostly serves to preserve charge neutrality inside the lattice, its size is critical because a bigger or smaller 'A'-site cation can cause the lattice to expand or shrink, resulting shift in the optical bandgap.(Borriello et al., 2008; He et al., 2021) When the tolerance factor (t) is between 0.813 and 1.107, the ideal perovskite structure is formed, leaving a very narrow range of permissible cationic radii ($r_A$) for 'A'-site cation in ABX₃ structure.(Li et al., 2008) Previously, it has been found that a slight addition of larger FA⁺ cation ($r_{FA}^+$ = 2.53 Å) into MAPbI₃ (where $r_{MA}^+$ = 2.17 Å) results in a mixed-phase MA/FAPbI₃ perovskite which further leads to enhance structural stability and extended light absorption in the near IR (infrared) region of the solar spectrum.(Eperon et al., 2014; Mahmud et al., 2016) Fig. 1b shows the UV–visible absorption spectra of the produced perovskite films, which shows a redshift in the absorption onset and a small improvement
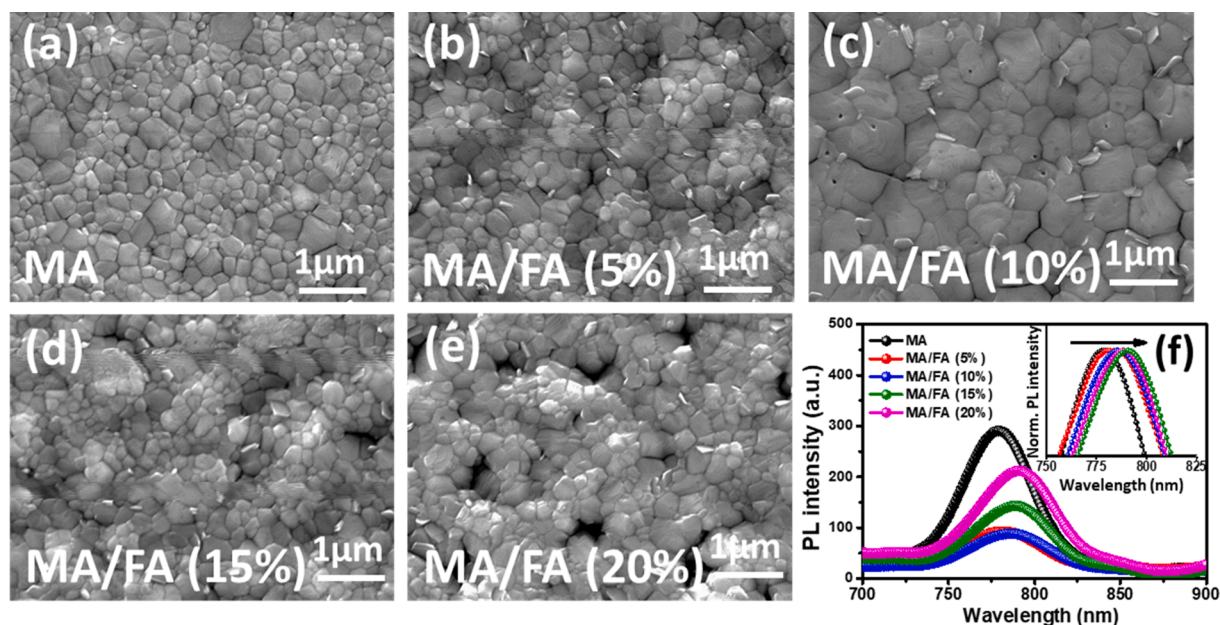
**Fig. 2.** **(a-e)** FESEM images of the MA/FAPbI₃ perovskite films prepared with varying concentrations of FAI and **(f)** shows the photoluminescence (PL) intensity of all the perovskite films coated on the glass and glass/ITO/SnO₂ substrates. The inset figure in (f) shows the shift in the PL peak position when PL intensity is normalized.

in the absorption over the visible region for the FA⁺ treated films. The energy bandgaps ($E_g$) of all the perovskite films were determined from the Tauc-plot **(Fig. 1c)**. The replacement of the 'A'-site MA⁺ cation with a bigger FA⁺ cation expands the perovskite lattice, thereby decreasing its $E_g$.(Eperon et al., 2014) The $E_g$ values of MA, MA/FA (5%), MA/FA (10%), MA/FA (15%), and MA/FA (20%) films have been calculated as 1.602, 1.586, 1.572, 1.567, and 1.563 eV, respectively. The X-ray diffraction (XRD) results shown in **Fig. 1d & 1e** have provided similar

evidence where the inclusion of FA⁺ cation at the 'A'-site of the perovskite lattice shifted the diffraction peak towards the lower angle side from 14.19° to 14.07°. The 'a' lattice parameter estimated from XRD (1 1 0) peaks was likewise shown to rise with increasing FA⁺ concentrations **(Fig. S1)**. The rising value of the lattice parameter shows that the crystal structure of the perovskites is transitioning from tetragonal (MAPbI₃) to intermediate quasi-cubic (MA/FAPbI₃) **(Fig. 1f)**.

The field emission scanning electron microscopy (FESEM) was used
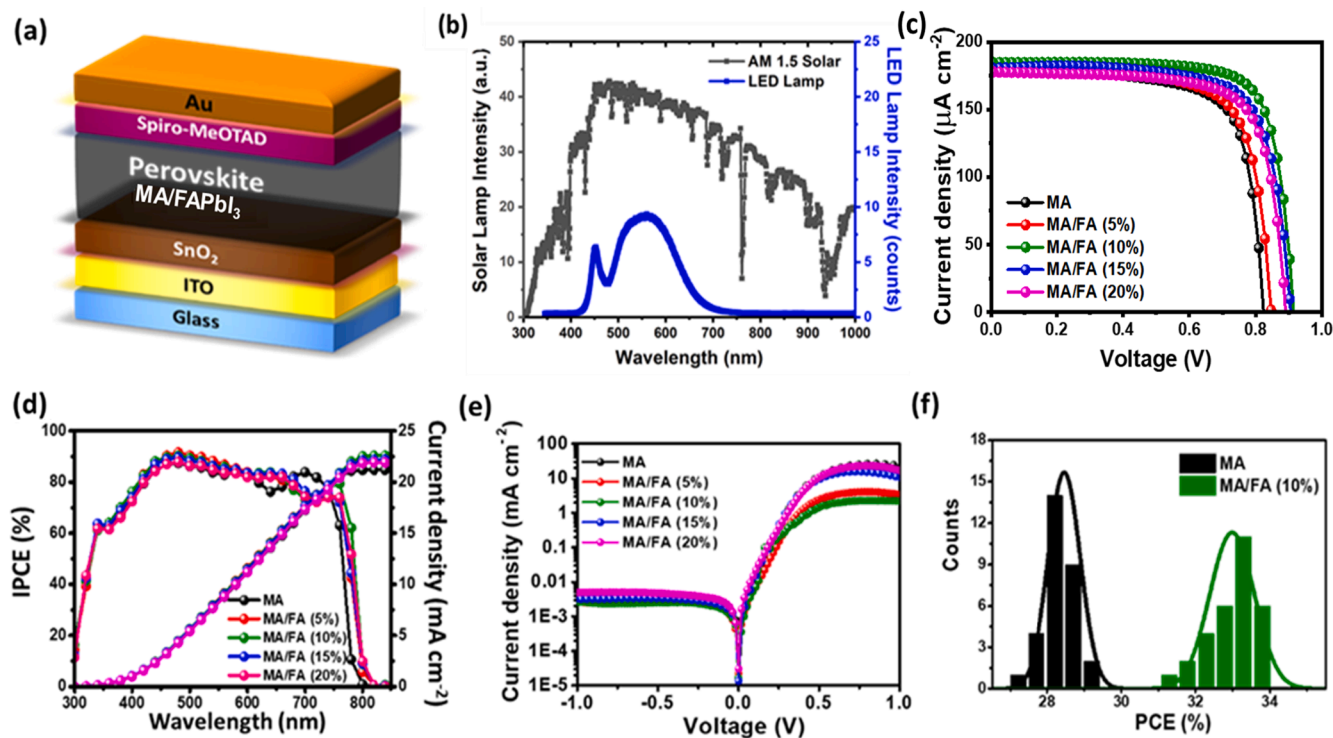


**Fig. 3.** (a) Layered structure of the fabricated i-PPVs, (b) irradiance spectra of various light sources used in this work; LED lamp (blue color) and solar AM 1.5 G lamp (black color), (c) *J–V* characteristics of i-PPVs under LED lamp at 1000 lux, (d) incident photon conversion efficiency (IPCE) spectra of i-PPVs. (e) dark current density ($J_d$) versus voltage, ($J_d$-$V$), and (f) statistical distribution of PCE of i-PPVs for the MAPbI₃ and MA/FAPbI₃ for an optimum concentration of FAI. (For interpretation of the references to color in this figure legend, the reader is referred to the web version of this article.)

**Table 1**

PV parameters of the fabricated i-PPVs characterized under an artificial indoor LED lamp source at 1000 lx.

| Perovskite | $V_{oc}$ (V) | $J_{sc}$ (μA cm$^{-2}$) | FF (%) | PCE (%) |
|---|---|---|---|---|
| MA | 0.83 | 178.46 | 72.06 | 28.63 |
| MA/FA (5%) | 0.86 | 180.55 | 74.14 | 30.04 |
| MA/FA (10%) | 0.92 | 186.52 | 74.16 | 34.07 |
| MA/FA (15%) | 0.91 | 179.70 | 75.23 | 31.56 |
| MA/FA (20%) | 0.90 | 175.46 | 73.48 | 31.24 |

to investigate the influence of varying FA$^+$ concentrations on MA/FAPbI$_3$ perovskite morphology (Fig. 2a-e). The reference MA film had compact morphology with smaller grains (Fig. 2a), which evolved into films with slightly larger grain sizes (MA/FA (5%) and MA/FA (10%)) due to the lattice expansion effect of the FA$^+$ cation (Fig. 2b-c). The densely packed larger grains morphology of the perovskite crystal leads to lower traps that reduces the recombination of excitons, resulting in enhanced $J_{SC}$ of the i-PPVs.(Lim et al., 2020; Long et al., 2017; Zhang et al., 2017) Further increase in concentration of FA$^+$ (15% and 20 %) cation resulted morphological deformation and increase in pinholes (Fig. 2d-e). The increase in defects/pinholes in perovskite film could increase the charge carrier recombination, resulting a drop in photovoltaic performance. Overall, optimum MA/FA (10%) concentration had the best morphology among all, with the biggest grain size, and their complementary effects can be seen in the photoluminescence (PL) spectra (Fig. 2f). In comparison to the reference MA film, the PL spectra for the perovskite films measured on glass/ITO/SnO$_2$ substrates have shown quenched and redshifted peaks for MA/FA perovskite films. The quenched PL peaks imply improved charge transfer from the perovskite layer to the SnO$_2$ electron transport layer (ETL) and the redshift in PL peaks is also supported by the absorption of the perovskite films.

## 2.2. Photovoltaic properties

The device structure of i-PPVs was glass/ITO/SnO$_2$/perovskite (MA/FAPbI$_3$)/spiro-MeOTAD/Au, as illustrated in Fig. 3a. Fig. S2 shows cross-sectional images of MA and MA/FA (10%) based devices. Fig. 3b presents the irradiance spectra of LED lamp (image of custom-designed indoor light setup is shown in Fig. S3) and conventional solar AM 1.5 G. Fig. 3c depicts the current-density versus voltage (*J-V*) characteristics of all fabricated i-PPVs under an indoor LED lamp at 1000 lx (0.326 mW cm$^{-2}$) with their PV parameters given in Table 1. The i-PPVs with the optimum perovskite absorber layer (MA/FA (10%)), had the best PCE of 34.07% along with a $V_{OC}$ of 0.92 V, short-circuit current density ($J_{SC}$) of 186.52 μA cm$^{-2}$, and fill factor (*FF*) of 74.16%, whereas i-PPVs with reference MAPbI$_3$ have a maximum PCE of 28.63% along with $V_{OC}$, $J_{SC}$, and *FF*, values of 0.83 V, 178.46 μA cm$^{-2}$, and 72.06%, respectively.

The incident photon conversion efficiency (IPCE) of the i-PPVs in Fig. 3d shows a slight enhancement over the visible region and the higher wavelength edge of the spectrum to redshift after the addition of FA$^+$ which is in agreement with the corresponding absorption spectra (Fig. 1b). To further evaluate the improved $V_{OC}$ of the i-PPVs, the change in the dark current density ($J_d$) with applied voltage was studied. For an ideal indoor PV with $R_{Sh} \gg R_s$ and photocurrent density ($J_{Ph}$) ($J_{Ph} = J_d$) the relationship between $J_d$ and $V_{OC}$ is given by $V_{OC} \approx \left(\frac{nkT}{q}\right) ln\left\{\frac{J_{SC}}{J_d}\right\}$, where n is the diode ideality factor, k is Boltzmann's constant, T is the temperature in Kelvin, and q is the elementary charge.(Parashar et al., 2021) This suggests that devices with a lower $J_d$ will have a better $V_{OC}$, as confirmed by the measured $J_d$–V of the optimized devices in Fig. 3e. Nevertheless, all of the i-PPVs showed reduced values of $J_d$ but the most reduced value of $J_d$ was observed for the MA/FA (10%) and its result was reflected in the $V_{OC}$ which was observed to be highest for this case as compared to other devices. Apart from $V_{OC}$, the addition of FA$^+$ had a significant effect on the $J_{SC}$ also due to lesser traps (discussed in the next section), enhanced absorption in the visible region, and improved charge transfer between SnO$_2$ ETL and perovskite layer as seen in the PL
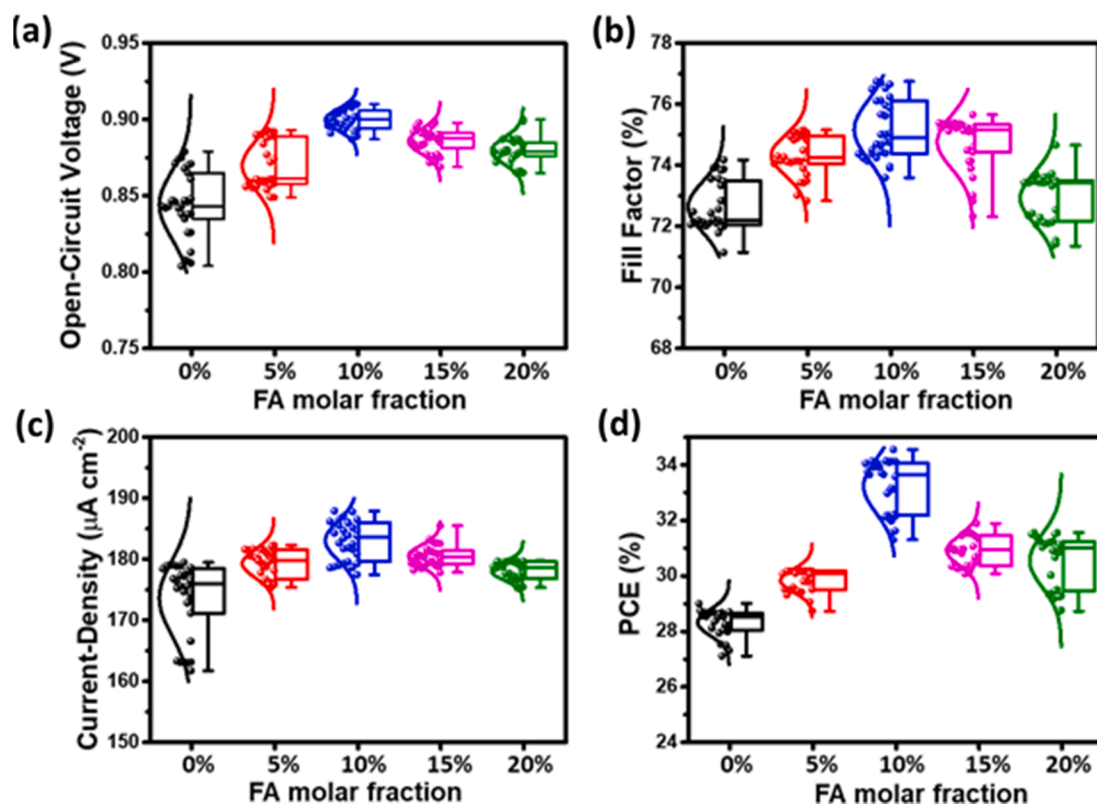


**Fig. 4.** Statistical distribution (a) $V_{OC}$, (b) *FF*, (c) $J_{SC}$, and (d) PCE for MA/FAPbI$_3$based i-PPVs under LED light source (1000 lx).
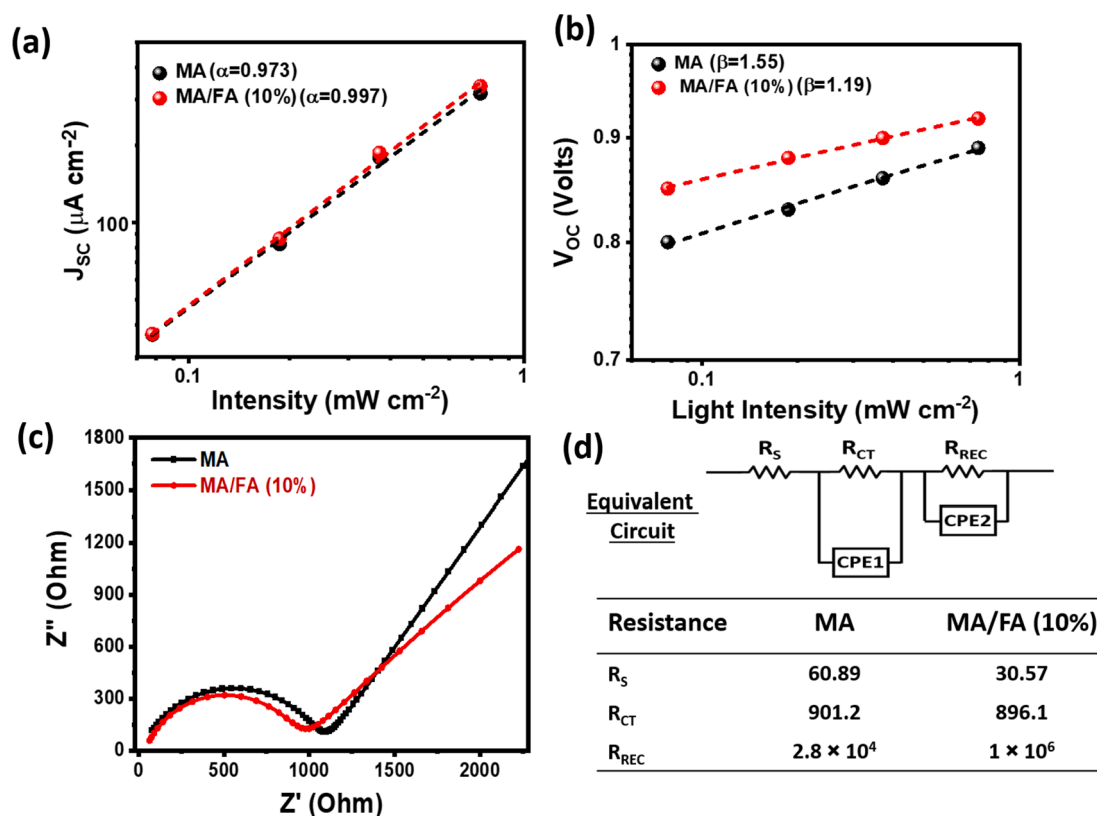
**Fig. 5.** (a) $J_{SC}$ vs light intensity and (b) $V_{OC}$ vs light intensity, *J-V* characteristics under different incident light intensity are shown in **Fig. S6** and results summarize in **Table S3**, (c) Nyquist plots and (d) equivalent circuit model used for data analysis and fitting results of impedance spectroscopy.

spectra (Fig. 2**f**).

Under the same experimental conditions, about 30 independent cells were fabricated to examine the reproducibility of the PV parameters. Fig. 3**f** shows the average PCE of $27.56 \pm 1.07$ for the reference structure of MA and $33.56 \pm 0.51\%$ for the optimum structure of MA/FA (10%). Fig. 4**a-d** shows the statistical data for the optimization of i-PPVs for PV parameters $V_{OC}$, *FF*, $J_{SC}$, and PCE. The constructed devices were also measured under conventional one-sun conditions for comparison. **Fig. S4**, **Table. S1** and **Fig. S5** show the *J-V* characteristics, PV parameters, and statistical distribution data under one-sun conditions, respectively.

### 2.3. Charge carrier recombination losses

The recombination losses were explored by measuring photovoltaic parameters ($J_{SC}$ and $V_{OC}$) under varying incident light intensities (*I*) and using impedance spectroscopy to investigate the variation in PV parameters of the reference MAPbI$_3$ and optimized MA/FAPbI$_3$ i-PPVs (Fig. 5**a-d**). Light intensity-dependent $J_{SC}$ curves were fitted with well-known power-law relationship, i.e. $J_{SC} \propto I^{\alpha}$, where α denotes the degree of bimolecular recombination (Kini et al., 2021; Koster et al., 2005). The α equal to 1 indicates that there is no bimolecular recombination, whereas 'α' value differs from 1 implying the existence of bimolecular recombination losses. Fitted data result α values of 0.997 for MA/FA (10%) indicate the lower bimolecular recombination rates relative to the 0.973 of MA-based reference i-PPVs. Meanwhile, the relationship between $V_{OC}$ and *I* gives information about the trap-assisted recombination losses which is $V_{OC} \propto \frac{\beta kT}{q} \ln(I)$ where the coefficient 'β' generally ranges between 1 and 2. The 'β' value equal to 1 indicates the absence of trap-assisted recombination, whereas $\beta > 1$ indicates the presence of trap states.(Sharma et al., 2021; Tress et al., 2018) Thus, results show that MA/FA (10%) with 'β' value of 1.19 has smaller trap-assisted

recombination losses as compared to MA with 'β' value of 1.55. Charge carrier dynamics at the interfaces of i-PPVs were also investigated using impedance spectroscopy (IS) under dark conditions(Hailegnaw et al., 2020), as seen in Fig. 5**c**, which shows Nyquist plots and Fig. 5**d** shows the equivalent circuit used to fit the IS data for MA and MA/FA (10%), respectively. Recombination occurs predominantly at the functional layer interface for PSCs, where electrons in the conduction band of the ETL or perovskite layer recombine with holes in the highest occupied molecular orbital (HOMO) energy level of the hole transport layer (HTL), the resistance that accounts for this is called recombination resistance ($R_{rec}$). It was found that the $R_{rec}$ for MA/FA ($10^6\ \Omega$) is 2 orders of magnitude higher than MAPbI$_3$ of $2.8 \times 10^4\ \Omega$, the higher value of $R_{rec}$ suggests lower recombination losses in MA/FA (10%) i-PPVs (Fig. 5**a-b**). Similarly, lower values of charge transfer resistance ($R_{ct}$) for MA/FA (896.1 Ω) compared to MAPbI$_3$ (901.2 Ω) support the better device performance of mixed cations perovskite.

### 2.4. Topography and defects at grain boundaries (GBs)

To further deeply investigate the morphological properties and surface potential (SP) of the MA and MA/FA (10%) perovskite films, atomic force microscopy (AFM) and kelvin probe force microscopy (KPFM) were used. Fig. 6**a & 6c** are the AFM micrographs, where MA/FA (10%) sample has a much lower average roughness ($R_{avg}$) of 17.1 nm than the reference MA perovskite film of 32.1 nm, which indicates that mixed cations result in a smoother perovskite surface (**Fig. S7**). The SP mapping at the same area of respective perovskites measured in the dark is presented in Fig. 6**b & 6d**. The grains and GBs can be easily differentiated via dark and bright portions of the obtained KPFM images, respectively. As defects i.e., vacancies and interstitials are more likely to be found at GBs leading to a significant difference in SP compared to the grains.(Lin et al., 2019; Tang et al., 2022; Zhang et al., 2015) In the MA/FA (10%) sample, the average SP is much smaller than the MA (~22.7
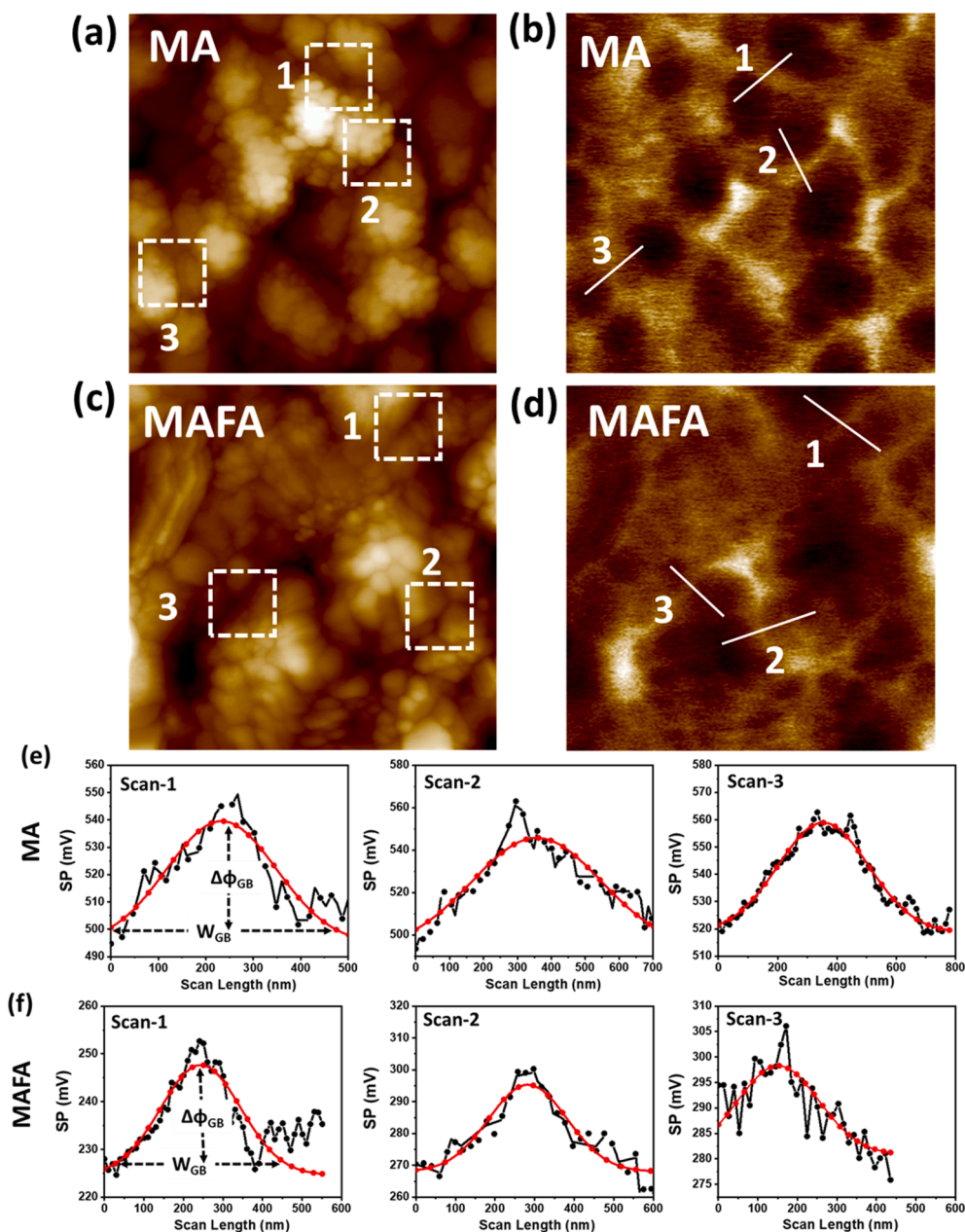
**Fig. 6.** AFM height images and surface potential (SP) mapping at the same topography images (a, b) MA and (c, d) MAFA perovskites. Marked dotted line square presents the selected grain boundaries and the solid line indicates the scan lines. Scanned profile for the (e) MA and (f) MA/FA (10%) of three different GBs. $\Delta\phi_{GB}$ and $W_{GB}$ were estimated and tabulated in Table 2.

**Table 2**
GB parameters ($\Delta\phi_{GB}$ and $W_{GB}$) were extracted from KPFM images of MA and MAFA at three randomly selected different grain boundaries.

| Perovskites | Parameters | Scan-1 | Scan-2 | Scan-3 | Avg. |
|---|---|---|---|---|---|
| **MA** | $\Delta\phi_{GB}$ (mV) | 44.82 | 52.26 | 40.28 | $45.8 \pm 6.1$ |
| | $W_{GB}$ (nm) | 584.6 | 648.5 | 701.4 | $644.8 \pm 58.5$ |
| **MA/FA (10%)** | $\Delta\phi_{GB}$ (mV) | 23.1 | 27.5 | 17.41 | $22.7 \pm 5.1$ |
| | $W_{GB}$ (nm) | 410.5 | 422.4 | 386.4 | $406 \pm 18.4$ |

mV compare to ∼ 45.8 mV) and SP variation across the GBs is also less apparent (Fig. 6e & 6f). Therefore, it can be inferred that defect (trapping states) have been reduced and passivated for mixed cation perovskite at GBs, where lower average SP barrier ($\Delta\phi_{GB}$) and smaller distribution width ($W_{GB}$) were found at GBs (Table 2). The transport of the charge carriers is obstructed at the GBs due to the $\Delta\phi_{GB}$ created by these defect states. Also, the reduced $\Delta\phi_{GB}$ implies an efficient charge transport in MA/FA (10%) perovskite film compared to MA. However, GBs in MA are more susceptible to defect states, which causes ion migration that leads to hysteresis in the *J-V* characteristics.(Kim et al., 2019; Sherkar et al., 2017) The defect states in MA are mostly interstitial and vacancies near the GB region mostly arise due to the smaller amount of ion formation energy.(Yin et al., 2014) Hence, these defects facilitate ion migration that is mainly present at GBs rather than the bulk of the grain.(Shao et al., 2016) This study reveals a decrease in defect concentration leads to insignificant hysteresis in MA/FA (10%) perovskites systems (**Fig. S8** & **Table. S2**).

Most of the nonradiative losses occur at the GBs due to the availability of charge carrier defects/trap states, therefore, optical and fluorescent mapping of the perovskite film coated on the glass substrates have been performed and respective PL spectrum (**Fig. S9**) were recorded. Recorded images have displayed significant variations in PL
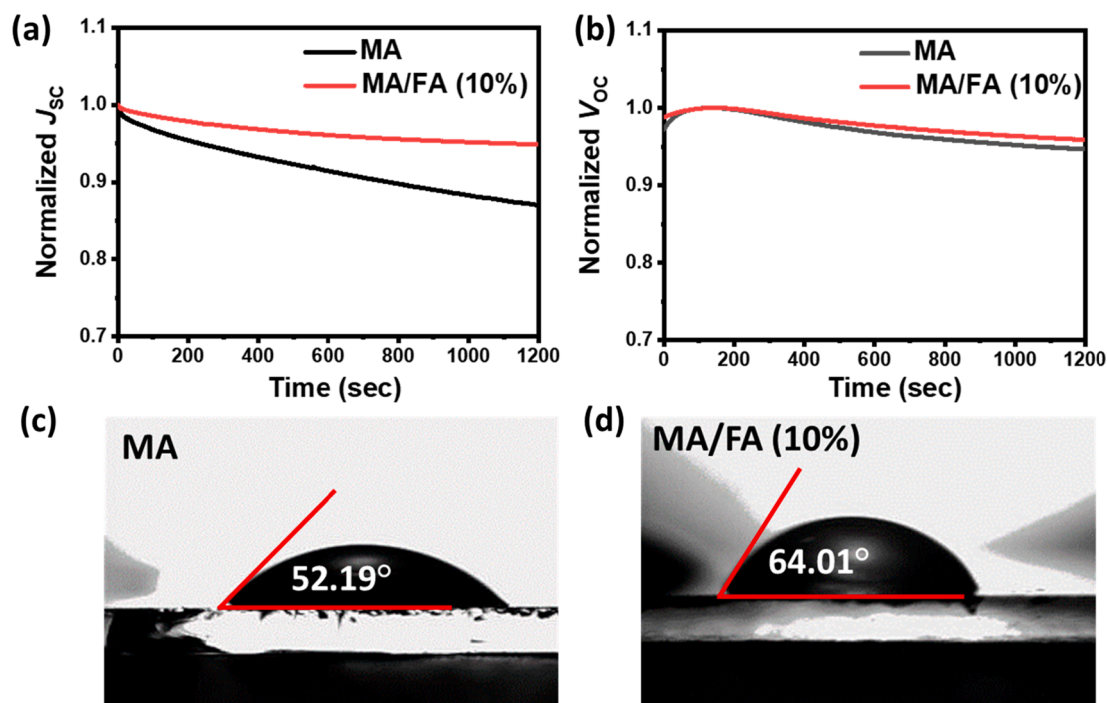
**Fig. 7.** Operation stability of the i-PPVs (a) $J_{SC}$ vs time and (b) $V_{OC}$ vs time under a continuous illumination from an LED at 1000 lx, and (c) contact angles measured for the water droplet on perovskite film.

intensity across grains and GBs. Generally, crystalline perovskite shows stronger emission when compared with amorphous components.(Kondo et al., 2010; Ummadisingu et al., 2017) Dark portion in the images indicates the defects or trap states at GBs and/or around the GBs. Fluorescent mapping of the perovskite film also supports the crystalline properties as well as trap-assisted recombination mechanism of the formulated system.

### 2.5. Operational stability of i-PPVs

The operational stability and suitability of the fabricated i-PPVs were investigated by recording the normalized $J_{SC}$ versus time (Fig. 7a) and $V_{OC}$ versus time (Fig. 7b) characteristics under a continuous illumination from an LED at 1000 lx (relative humidity (RH) level of the cleanroom during characterization was at 33%). The i-PPVs with MA/FA (10%) have shown the most stabilized trend of $J_{SC}$ and $V_{OC}$ as compared to other i-PPVs. The stable trend of $J_{SC}$ and $V_{OC}$ indicates that the FA$^+$ addition in MAPbI$_3$ stabilizes the crystal structure of the perovskite as well. Additionally, the operational stability of the fabricated i-PPVs was also studied under the standard one-sun conditions (Fig. S10) which confirms the same trend for $J_{SC}$ and $V_{OC}$ under the one-sun conditions as observed under the indoor lighting conditions for all sets of devices.

To investigate the hydrophobicity of the perovskite layers, contact angles were measured between a water droplet and the fabricated perovskite films (Fig. 7c-d). The reference MA film had the smallest contact angle of 52.19° as compared to 54.85°, 64.01°, 49.64°, and 40.61° for MA/FA (5%), MA/FA (10%), MA/FA (15%), and MA/FA (20%), respectively. Thus, MA/FA (10%) film was the most moisture resistive as compared to the other perovskite films. The decrease in contact angles for films with more concentration of FA$^+$ might be due to the rough film and pinholes in morphology which might affect the angle between the water droplet and the perovskite film. Overall, based on the above results it can be concluded that the quasi-cubic perovskite structure formed after the FA$^+$ addition is much more stable in every aspect as compared to the pristine MAPbI$_3$ perovskite.

### 3. Conclusion

In summary, the role of a larger FA$^+$ cation in the MAPbI$_3$ perovskite to fabricate a mixed cation quasi-cubic MA/FAPbI$_3$ perovskite structure has been explored. The FA$^+$ cation plays an important role in adjusting the lattice parameters of the perovskite crystal and expands the lattice from tetragonal (MAPbI$_3$) to quasi-cubic structure (MA/FAPbI$_3$). An optimal concentration of FA$^+$ (10 mol %) can be used to achieve a stable quasi-cubic perovskite structured perovskite which delivered an outstanding PCE of 34.07% as compared to the reference MAPbI$_3$ based i-PPVs (PCE = 28.63%) under indoor LED light source at 1000 lx. The effect of quasi-cubic mixed cation perovskite on the absorption, morphology, charge transport, and trap states was examined in detail and a vivid narrative has been provided on the device physics under indoor lighting conditions. In addition, the variation in surface potential and fluorescent microscopy imaging firmly confirms the lesser defects at grain boundaries for mixed cation-based perovskite. In comparison to previous research, it was observed that altering the 'A'-site cation in i-PPVs to tune the crystal structure is more advantageous than changing the ratio of halides in the perovskite layer. Thus, the stable and efficient quasi-cubic structured mixed cations perovskite materials are much more suitable choices for indoor applications.

### Declaration of Competing Interest

The authors declare that they have no known competing financial interests or personal relationships that could have appeared to influence the work reported in this paper.

## Appendix A. Supplementary data

Supplementary data to this article can be found online at https://doi.org/10.1016/j.solener.2022.09.015.

## References

Aslam, A., Mehmood, U., Arshad, M.H., Ishfaq, A., Zaheer, J., Ul Haq Khan, A., Sufyan, M., 2020. Dye-sensitized solar cells (DSSCs) as a potential photovoltaic technology for the self-powered internet of things (IoTs) applications. Solar Energy 207, 874-892.

Borriello, I., Cantele, G., Ninno, D., 2008. Ab initio investigation of hybrid organic-inorganic perovskites based on tin halides. Phys. Rev. B 77 (23), 235214.

Chen, C.-Y., Chang, J.-H., Chiang, K.-M., Lin, H.-L., Hsiao, S.-Y., Lin, H.-W., 2015. Perovskite Photovoltaics for Dim-Light Applications. Adv. Funct. Mater. 25 (45), 7064–7070.

Cheng, R., Chung, C.-C., Zhang, H., Liu, F., Wang, W.-T., Zhou, Z., Wang, S., Djurišić, A. B., Feng, S.-P., 2019. Tailoring Triple-Anion Perovskite Material for Indoor Light Harvesting with Restrained Halide Segregation and Record High Efficiency Beyond 36%. Adv. Energy Mater. 9 (38), 1901980. https://doi.org/10.1002/aenm.201901980.

Dagar, J., Castro-Hermosa, S., Lucarelli, G., Cacialli, F., Brown, T.M., 2018. Highly efficient perovskite solar cells for light harvesting under indoor illumination via solution processed SnO$_2$/MgO composite electron transport layers. Nano Energy 49, 290–299.

Dong, Q., Fang, Y., Shao, Y., Mulligan, P., Qiu, J., Cao, L., Huang, J., 2015. Electron-hole diffusion lengths > 175 μm in solution-grown CH$_3$NH$_3$PbI$_3$ single crystals. Science 347 (6225), 967–970.

Eperon, G.E., Stranks, S.D., Menelaou, C., Johnston, M.B., Herz, L.M., Snaith, H.J., 2014. Formamidinium lead trihalide: a broadly tunable perovskite for efficient planar heterojunction solar cells. Energy Environ. Sci. 7 (3), 982–988.

Green, M., Dunlop, E., Hohl-Ebinger, J., Yoshita, M., Kopidakis, N., Hao, X., 2021. Solar cell efficiency tables (version 57). Prog. Photovoltaics Res. Appl. 29 (1), 3–15.

Guo, Y., Sato, W., Shoyama, K., Halim, H., Itabashi, Y., Shang, R., Nakamura, E., 2017. Citric Acid Modulated Growth of Oriented Lead Perovskite Crystals for Efficient Solar Cells. J. Am. Chem. Soc. 139 (28), 9598–9604.

Guo, Z., Jena, A.K., Takei, I., Ikegami, M., Ishii, A., Numata, Y., Shibayama, N., Miyasaka, T., 2021. Dopant-Free Polymer HTM-Based CsPbI2Br Solar Cells with Efficiency Over 17% in Sunlight and 34% in Indoor Light. Adv. Funct. Mater. 31 (42), 2103614. https://doi.org/10.1002/adfm.202103614.

Hailegnaw, B., Sariciftci, N.S., Scharber, M.C., 2020. Impedance Spectroscopy of Perovskite Solar Cells: Studying the Dynamics of Charge Carriers Before and After Continuous Operation. Physica Status Solidi (a) 217 (22), 2000291.

He, R., Ren, S., Chen, C., Yi, Z., Luo, Y., Lai, H., Wang, W., Zeng, G., Hao, X., Wang, Y., Zhang, J., Wang, C., Wu, L., Fu, F., Zhao, D., 2021. Wide-bandgap organic–inorganic hybrid and all-inorganic perovskite solar cells and their application in all-perovskite tandem solar cells. Energy Environ. Sci. 14 (11), 5723–5759.

Kawata, K., Tamaki, K., Kawaraya, M., 2015. Dye-sensitised and Perovskite Solar Cells as Indoor Energy Harvestors. J. Photopolym. Sci. Technol. 28 (3), 415–417.

Kim, S., Yun, J.S., Sharma, P., Lee, D.S., Kim, J., Soufiani, A.M., Huang, S., Green, M.A., Ho-Baillie, A.W.Y., Seidel, J., 2019. Light- and bias-induced structural variations in metal halide perovskites. Nat. Commun. 10 (1), 444.

Kini, G.P., Parashar, M., Shukla, V.K., Singh, R., 2021. Deciphering the effect of replacing thiophene with selenophene in diketopyrrolopyrrole (DPP)-based low cost hole transport materials on the performance of perovskite solar cells. Sustainable Energy Fuels 5 (23), 5994–6003.

Kondo, S., Ohsawa, H., Asada, H., Saito, T., 2010. Inherent excitonic luminescence in metal halide promising for potential applications in light-emitting devices. J. Appl. Phys. 107 (10), 103526.

Koster, L.J.A., Mihailetchi, V.D., Xie, H., Blom, P.W.M., 2005. Origin of the light intensity dependence of the short-circuit current of polymer/fullerene solar cells. Appl. Phys. Lett. 87 (20), 203502.

Lee, M., Choi, E., Soufiani, A.M., Lim, J., Kim, M., Chen, D., Green, M.A., Seidel, J., Lim, S., Kim, J., Dai, X., Lee-Chin, R., Zheng, B., Hameiri, Z., Park, J., Hao, X., Yun, J. S., 2021. Enhanced Hole-Carrier Selectivity in Wide Bandgap Halide Perovskite Photovoltaic Devices for Indoor Internet of Things Applications. Adv. Funct. Mater. 31 (16), 2008908.

Li, C., Lu, X., Ding, W., Feng, L., Gao, Y., Guo, Z., 2008. Formability of ABX$_3$ (X = F, Cl, Br, I) halide perovskites. Acta Crystallogr. Sect. B 64 (6), 702–707.

Lim, J.W., Kwon, H., Kim, S.H., You, Y.-J., Goo, J.S., Ko, D.-H., Lee, H.J., Kim, D., Chung, I., Kim, T.G., Kim, D.H., Shim, J.W., 2020. Unprecedentedly high indoor performance (efficiency > 34 %) of perovskite photovoltaics with controlled bromine doping. Nano Energy 75, 104984.

Lin, L., Wang, J.-T.-W., Jones, T.W., Grigore, M., Cook, A., deQuilettes, D.W., Brenes, R., Duck, B.C., Anderson, K.F., Duffy, N.W., Wenger, B., Bulović, V., Pu, J., Li, J., Chi, B., Snaith, H.J., Wilson, G.J., 2019. Bulk recrystallization for efficient mixed-cation mixed-halide perovskite solar cells. J. Mater. Chem. A 7 (44), 25511–25520.

Liu, T., Lai, H., Wan, X., Zhang, X., Liu, Y., Chen, Y., 2018. Cesium Halides-Assisted Crystal Growth of Perovskite Films for Efficient Planar Heterojunction Solar Cells. Chem. Mater. 30 (15), 5264–5271.

Long, M., Zhang, T., Xu, W., Zeng, X., Xie, F., Li, Q., Chen, Z., Zhou, F., Wong, K.S., Yan, K., Xu, J., 2017. Large-Grain Formamidinium PbI$_{3-x}$Br$_x$ for High-Performance

Perovskite Solar Cells via Intermediate Halide Exchange. Adv. Energy Mater. 7 (12), 1601882.

Mahmud, M.A., Elumalai, N.K., Upama, M.B., Wang, D., Wright, M., Chan, K.H., Xu, C., Haque, F., Uddin, A., 2016. Single Vs Mixed Organic Cation for Low Temperature Processed Perovskite Solar Cells. Electrochim. Acta 222, 1510–1521.

Mathews, I., King, P.J., Stafford, F., Frizzell, R., 2016. Performance of III–V Solar Cells as Indoor Light Energy Harvesters. IEEE J. Photovoltaics 6 (1), 230–235.

Muhammad, B.T., Kar, S., Stephen, M., Leong, W.L., 2022. Halide perovskite-based indoor photovoltaics: recent development and challenges. Mater. Today Energy 23, 100907.

Nazeeruddin, M.K., Snaith, H., 2015. Methylammonium lead triiodide perovskite solar cells: A new paradigm in photovoltaics. MRS Bull. 40 (8), 641–645.

Noh, Y.W., Jin, I.S., Kim, K.S., Park, S.H., Jung, J.W., 2020. Reduced energy loss in SnO2/ZnO bilayer electron transport layer-based perovskite solar cells for achieving high efficiencies in outdoor/indoor environments. J. Mater. Chem. A 8 (33), 17163–17173.

Parashar, M., Singh, R., Yoo, K., Lee, J.-J., 2021. Formation of 1-D/3-D Fused Perovskite for Efficient and Moisture Stable Solar Cells. ACS Appl. Energy Mater. 4 (3), 2751–2760.

Park, N.-G., 2015. Perovskite solar cells: an emerging photovoltaic technology. Mater. Today 18 (2), 65–72.

Pham, H.D., Jain, S.M., Li, M., Wang, Z.-K., Manzhos, S., Feron, K., Pitchaimuthu, S., Liu, Z., Motta, N., Durrant, J.R., Sonar, P., 2020. All-Rounder Low-Cost Dopant-Free D-A-D Hole-Transporting Materials for Efficient Indoor and Outdoor Performance of Perovskite Solar Cells. Adv. Electron. Mater. 6 (4), 1900884.

Ren, A., Lai, H., Hao, X., Tang, Z., Xu, H., Yu Jeco, B.M.F., Watanabe, K., Wu, L., Zhang, J., Sugiyama, M., Wu, J., Zhao, D., 2020. Efficient Perovskite Solar Modules with Minimized Nonradiative Recombination and Local Carrier Transport Losses. Joule 4 (6), 1263–1277.

Saranin, D., Komaricheva, T., Luchnikov, L., Muratov, D.S., Le, T.S., Karpov, Y., Gostishchev, P., Yurchuk, S., Kuznetsov, D., Didenko, S., Di Carlo, A., 2021. Hysteresis-free perovskite solar cells with compact and nanoparticle NiO for indoor application. Sol. Energy Mater. Sol. Cells 227, 111095.

Savenije, T.J., Ponseca, C.S., Kunneman, L., Abdellah, M., Zheng, K., Tian, Y., Zhu, Q., Canton, S.E., Scheblykin, I., Pullerits, T., Yartsev, A., Sundström, V., 2014. Thermally Activated Exciton Dissociation and Recombination Control the Carrier Dynamics in Organometal Halide Perovskite. J. Phys. Chem. Lett. 5 (13), 2189–2194.

Shao, Y., Fang, Y., Li, T., Wang, Q., Dong, Q., Deng, Y., Yuan, Y., Wei, H., Wang, M., Gruverman, A., Shield, J., Huang, J., 2016. Grain boundary dominated ion migration in polycrystalline organic–inorganic halide perovskite films. Energy Environ. Sci. 9 (5), 1752–1759.

Sharma, A., Singh, R., Kini, G.P., Hyeon Kim, J., Parashar, M., Kim, M., Kumar, M., Kim, J.S., Lee, J.-J., 2021. Side-Chain Engineering of Diketopyrrolopyrrole-Based Hole-Transport Materials to Realize High-Efficiency Perovskite Solar Cells. ACS Appl. Mater. Interfaces 13 (6), 7405–7415.

Sherkar, T.S., Momblona, C., Gil-Escrig, L., Ávila, J., Sessolo, M., Bolink, H.J., Koster, L.J. A., 2017. Recombination in Perovskite Solar Cells: Significance of Grain Boundaries, Interface Traps, and Defect Ions. ACS Energy Lett. 2 (5), 1214–1222.

Singh, R., Parashar, M., Sandhu, S., Yoo, K., Lee, J.-J., 2021. The effects of crystal structure on the photovoltaic performance of perovskite solar cells under ambient indoor illumination. Sol. Energy 220, 43–50.

Stranks, S.D., Eperon, G.E., Grancini, G., Menelaou, C., Alcocer, M.J.P., Leijtens, T., Herz, L.M., Petrozza, A., Snaith, H.J., 2013. Electron-Hole Diffusion Lengths Exceeding 1 Micrometer in an Organometal Trihalide Perovskite Absorber. Science 342 (6156), 341–344.

Tang, J., Wang, Y., Jiang, Y., Yao, J., Zhang, H., 2022. Solute Segregation to Grain Boundaries in Al: A First-Principles Evaluation. Acta Metallurgica Sinica (English Letters).

Tress, W., Yavari, M., Domanski, K., Yadav, P., Niesen, B., Correa Baena, J.P., Hagfeldt, A., Graetzel, M., 2018. Interpretation and evolution of open-circuit voltage, recombination, ideality factor and subgap defect states during reversible light-soaking and irreversible degradation of perovskite solar cells. Energy Environ. Sci. 11 (1), 151–165.

Ummadisingu, A., Steier, L., Seo, J.-Y., Matsui, T., Abate, A., Tress, W., Grätzel, M., 2017. The effect of illumination on the formation of metal halide perovskite films. Nature 545 (7653), 208–212.

Uslu, B.Ç., Okay, E., Dursun, E., 2020. Analysis of factors affecting IoT-based smart hospital design. Journal of Cloud Computing 9 (1), 67.

Venkateswararao, A., Ho, J.K.W., So, S.K., Liu, S.-W., Wong, K.-T., 2020. Device characteristics and material developments of indoor photovoltaic devices. Materials Science and Engineering: R: Reports 139, 100517.

Wetzelaer, G.-J.-A.-H., Scheepers, M., Sempere, A.M., Momblona, C., Ávila, J., Bolink, H. J., 2015. Trap-Assisted Non-Radiative Recombination in Organic-Inorganic Perovskite Solar Cells. Adv. Mater. 27 (11), 1837–1841.

Yin, W.-J., Shi, T., Yan, Y., 2014. Unusual defect physics in CH$_3$NH$_3$PbI$_3$ perovskite solar cell absorber. Appl. Phys. Lett. 104 (6), 063903.

Zhang, W., Pathak, S., Sakai, N., Stergiopoulos, T., Nayak, P.K., Noel, N.K., Haghighirad, A.A., Burlakov, V.M., deQuilettes, D.W., Sadhanala, A., Li, W., Wang, L., Ginger, D.S., Friend, R.H., Snaith, H.J., 2015. Enhanced optoelectronic quality of perovskite thin films with hypophosphorous acid for planar heterojunction solar cells. Nat. Commun. 6 (1), 10030.

Zhang, Y., Grancini, G., Feng, Y., Asiri, A.M., Nazeeruddin, M.K., 2017. Optimization of Stable Quasi-Cubic FA$_x$MA$_{1-x}$PbI$_3$ Perovskite Structure for Solar Cells with Efficiency beyond 20%. ACS Energy Lett. 2 (4), 802–806.